Parameter Independent Control of Doubly-Fed Reluctance Wind Generators without a Rotor Position Sensor

M. R. Agha Kashkooli[a,*], Milutin G. Jovanović[a]

[a]*Faculty of Engineering and Environment, Northumbria University, Newcastle upon Tyne, United Kingdom*

ABSTRACT

A novel model reference adaptive system (MRAS) based estimation technique for sensorless operation of a brushless doubly fed reluctance generator (BDFRG) with maximum power point tracking (MPPT) is proposed. The main advantage of this development is the truly machine parameter independent rotor angular velocity MRAS observer complemented by an original position error compensation scheme for higher accuracy, making it clearly superior to the existing designs. The simulation and experimental results have demonstrated the excellent performance prospects for typical wind turbines emulated in a laboratory environment.

Keywords: Brushless Doubly Fed Reluctance Generator; Wind Energy Conversion Systems; Sensorless Control.

1. Introduction

A doubly fed induction generator (DFIG) has been a popular choice of wind turbine manufacturers for variable speed wind energy conversion systems (e.g. 2:1 or so), especially in off-shore applications [1, 2]. However, the cost benefits of a 30% rated converter and its low failure rates are compromised by reliability and maintenance issues with brushes and slip-rings [3–5].

The emerging BDFRG, conceptually shown in Fig. 1, is a promising medium-speed alternative to DFIG [6, 7]. It can use a similar partially-rated converter, contributing further with reliability and maintenance advantages of brushless structure over DFIG [8]. The BDFRG has two stator windings of different pole numbers and frequencies: the grid-connected primary, and the back-to-back converter-fed secondary to enable a bi-directional power flow by analogy to the DFIG's rotor winding [9]. The magnetic coupling between them is achieved through a modern reluctance rotor having half the total number of the stator poles [10]. Such unusual design and operating principles make the BDFRG's 'natural' synchronous speed half the DFIG's for the same number of rotor poles and line frequency. Therefore, a simpler and more compact two-stage gearbox can be used for BDFRG wind turbines instead of a failures prone three-stage counterpart of DFIG, bringing extra economic benefits [6, 11]. The BDFRG also has preferable grid-integration properties to DFIG including a potentially crowbar-less inverter protection for low voltage ride through (afforded by the higher leakage inductances, hence the lower fault currents) and competitive frequency support [12, 13].

By virtues of the fixed switching rates and low total harmonic distortion, vector control has been a prevailing solution for wind energy conversion systems (WECS) either using the commercial DFIG [14, 15] or BDFRG prototypes [16, 17]. Shaft encoders, usually required for this purpose, raise reliability and maintenance concerns, increasing the WECS running costs. The development of various sensorless control strategies for both DFIG [18–21] and BDFRG [22–25] has been therefore gaining a lot in popularity recently.

A viable rotor angular position and velocity state observer has been applied for flux (field) oriented control of the BDFRG in [22, 23]. However, the effects of machine parameter knowledge inaccuracies have neither been addressed nor substantiated in this work. The MRAS based substitutes using the same control method as in [23] have been proposed in [24] and [25]. The troublesome secondary-flux estimation at typically low fundamental frequencies and PWM terminal voltages have precluded the controller stability over the whole speed range [24]. The performance boost has been accomplished using the secondary real power as a reference model foundation [25]. Although the adaptive model in [25] is dependent on both the secondary winding resistance (R_s) and mutual inductance (L_m), the sensitivity studies to R_s uncertainties have only been undertaken, but not to L_m variations playing a pivotal role for

*Corresponding author

mohammad.kashkooli@northumbria.ac.uk (M. R. Agha Kashkooli)

ORCID(s): 0000-0001-7511-2910 (M. R. Agha Kashkooli)

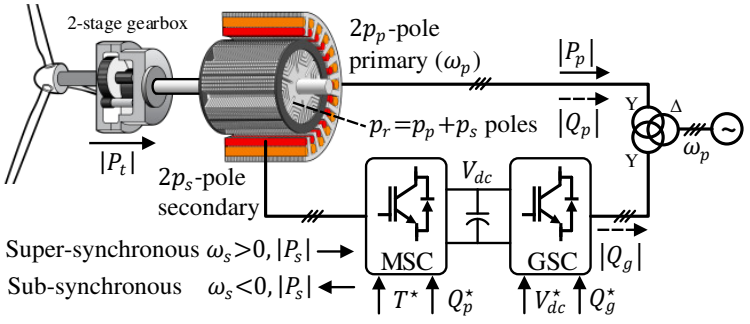

Figure 1: An outline of the BDFRG wind turbine drive train.

Table 1
Comparisons of the existing BDFRG sensorless methods

Method	Dependency	Flux observer	Vector control	Compensation	Application
[23]	L_m, L_p, R_p, J	Primary	Field orientated	No	Small-scale
[24]	L_m, L_s, R_s	Secondary	Field orientated	No	Small-scale
[25]	L_m, R_s	–	Field orientated	No	Small-scale
[26–28]	L_m, L_p, R_p	Primary	Voltage orientated	No	Small-scale
[29]	L_m, L_p	–	Voltage orientated	No	Large-scale
Proposed	–	–	Voltage orientated	Yes	Large-scale

the convergence of the underlying estimation process. The MRAS observers introduced in [26–28] use the measured secondary currents as the reference model outputs, while the corresponding estimates are entirely based on the primary quantities at fixed line-frequency. The integration technique for the primary-flux identification and knowledge of the primary winding resistance and inductances are the main drawbacks of the introduced adaptive models. Furthermore, the associated simulation results are produced for a small BDFRG prototype without modelling the aerodynamics of a WECS. The use of measured primary power in the adaptive model to obtain the secondary current estimates as presented in [29] avoids the flux calculation and primary resistance knowledge. However, the position estimation accuracy is affected by mismatch between the actual primary and mutual inductances and their off-line tested values.

A new, closed-loop rotor speed and position MRAS observer for inherently decoupled torque and reactive power control of the large-scale BDFRG without a shaft sensor has been proposed and evaluated. The measurable stationary frame secondary currents have served as the reference model outputs, providing the necessary stability and transducer-alike accuracy. Furthermore, the grid voltage and current measurements from the primary side have been merely used by the adaptive model to generate the corresponding high quality estimates. The observer design has been additionally refined by implementing an innovative on-line position error compensation algorithm for further performance improvements. The obtained parameter-free estimator is therefore much more robust and accurate than the parameter dependent alternatives, the Luenberger observer considered in [22, 23] and the MRAS counterparts discussed in [24, 25, 29]. Besides, the maximum torque per inverter ampere (MTPIA) strategy investigated in [23–25] requires the machine to be entirely magnetised by the primary winding, compromising the overall power factor of the BDFRG. As such, it is of little practical interest for large-scale applications under consideration in this paper. The aforementioned observer-controller attributes have been underpinned by realistic simulations and hardware-in-the-loop test results for a 1.5 MW BDFRG wind turbine. The comparative properties of the underlying MRAS approach and the other sensorless schemes documented in the literature are summarised in Table 1.

2. BDFRG Preliminaries

The BDFRG rotor angular velocity is given by [16, 17]:

$$\omega_{rm} = \frac{\omega_p + \omega_s}{p_r} = \frac{\omega_p}{p_r}\left(1 + \frac{\omega_s}{\omega_p}\right) = \omega_{syn}\left(1 + \frac{\omega_s}{\omega_p}\right) \tag{1}$$

If the secondary winding is DC (i.e $\omega_s = 0$), the BDFRG is in synchronous mode running at $\omega_{syn} = \omega_p/p_r$, which is half that of a p_r-pole DFIG given (1). Thus, the BDFRG is a medium-speed machine requiring a two-stage gearbox and avoiding the vulnerable high speed (3rd) stage of DFIG [3].

Using (1), the BDFRG mechanical power relationships in steady-state become as follows:

$$P_m = T_e \cdot \omega_{rm} = \underbrace{\frac{T_e \cdot \omega_p}{p_r}}_{P_p} + \underbrace{\frac{T_e \cdot \omega_s}{p_r}}_{P_s} = P_{s,p} \cdot \left(1 + \frac{\omega_{p,s}}{\omega_{s,p}}\right) \tag{2}$$

where the electro-magnetic torque, $T_e < 0$, and the primary power, $P_p < 0$ (i.e. $|P_p|$ delivered to the grid), with the adopted *motoring* (BDFRM) convention. Note from (2) and Fig. 1 that the secondary power flow (P_s) can be bi-directional: at super-synchronous speeds $\omega_s > 0$ and $P_s < 0$ (i.e. $|P_s|$ to the grid), and in sub-synchronous region $\omega_s < 0$ (meaning the opposite phase sequence of the secondary to the primary winding) for $P_s > 0$. The latter speed mode is apparently inefficient as the portion of P_p is being circulated through the machine via the converter producing losses on its way.

The BDFRG speed ratio for a given range around ω_{syn} mid point can be written as:

$$a = \frac{\omega_{max}}{\omega_{min}} = \frac{\omega_{syn} + \Delta\omega}{\omega_{syn} - \Delta\omega} = \frac{\omega_p + \omega_s}{\omega_p - \omega_s} \Longrightarrow \frac{\omega_s}{\omega_p} = \frac{a-1}{a+1} \tag{3}$$

Hence, for a typical $a = 2$, the maximum secondary frequency is $\omega_s = \omega_p/3$ and $P_s \approx 0.25 P_m$ according to (2). This means that ideally only a 25% rated converter would do as with the DFIG. Further details about the BDFRG operating principles and space-vector theory can be found in [30, 31].

3. Vector Control Principles

The BDFRM(G) $d-q$ model equations for the *p*rimary and *s*econdary windings in rotating reference frames (Fig. 2) using standard notation in complex form are [16, 17]:

$$\underline{v}_{p,s} = R_{p,s}\underline{i}_{p,s} + \frac{d\underline{\lambda}_{p,s}}{dt} + j\omega_{p,s}\underline{\lambda}_{p,s} \tag{4}$$

$$\underline{\lambda}_p = L_p\underline{i}_p + L_m\underline{i}^*_{sm} = L_p(i_{pd} + ji_{pq}) + L_m(i_{md} - ji_{mq}) \tag{5}$$

$$\underline{\lambda}_s = L_s\underline{i}_s + L_m\underline{i}^*_{pm} = \sigma L_s\underline{i}_s + \frac{L_m}{L_p}\underline{\lambda}^*_p = \sigma L_s\underline{i}_s + \underline{\lambda}_m \tag{6}$$

$$T_e = \frac{3}{2}p_r\left(\lambda_{pd}i_{pq} - \lambda_{pq}i_{pd}\right) = \frac{3}{2}p_r\left(\lambda_{md}i_{sq} - \lambda_{mq}i_{sd}\right) \tag{7}$$

$$Q_p = \frac{3}{2}\left(v_{pq}i_{pd} - v_{pd}i_{pq}\right) \tag{8}$$

where $L_{m,p,s}$ are the 3-phase magnetising and self inductances, $\sigma = 1 - L_m^2/(L_pL_s)$ is the leakage coefficient, λ_m is the mutual flux linkage, and $\underline{i}_{sm}$ is the frequency modulated secondary current vector ($\underline{i}_s$) rotating at ω_p and ω_s, respectively, as shown in Fig. 2. The following flux oriented control form relationships hold [16, 17, 23]:

$$\underbrace{\underline{i}_{sm} = i_{md} + ji_{mq} = i_{sm}e^{j\gamma}}_{d_p-q_p\,frame} \Leftrightarrow \underbrace{\underline{i}_s = i_{sd} + ji_{sq} = i_se^{j\gamma}}_{d_s-q_s\,frame} \tag{9}$$

Under the primary voltage alignment conditions (i.e $v_{pq} = v_p$, $v_{pd} = 0$) depicted in Fig. 2, ignoring the winding resistance (R_p), which is justified for MW range generators, and substituting (4) and (5) for $\lambda_{pd} \approx \lambda_p = v_p/\omega_p$, $\lambda_{pq} \approx 0$, with $i_{md} = i_{sd}$ and $i_{mq} = i_{sq}$ from (9), into (7) and (8), T_e and the primary reactive power (Q_p) in terms of the controllable secondary $d_s - q_s$ frame currents can be expressed as:

$$T_e = \frac{3}{2}p_r\lambda_p i_{pq} \approx \frac{3}{2}p_r \cdot \frac{v_p}{\omega_p} \cdot \frac{L_m}{L_p}i_{sq} \tag{10}$$

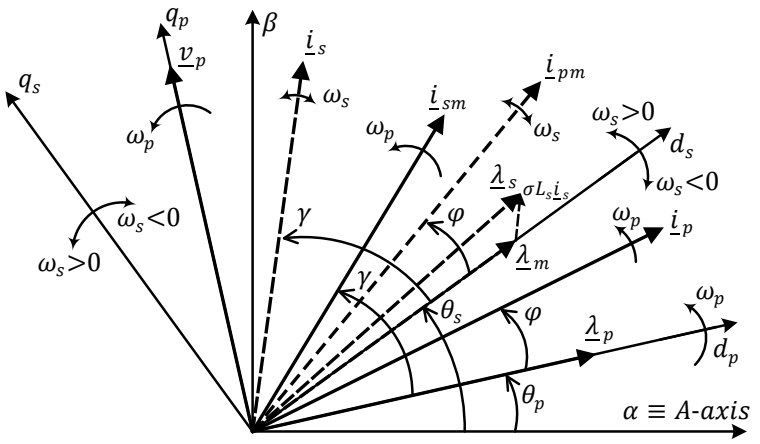

Figure 2: The BDFRG phasor diagram.

$$Q_p = \frac{3}{2} v_p i_{pd} \approx \frac{3 v_p}{2 L_p} \left(\frac{v_p}{\omega_p} - L_m i_{sd} \right) \tag{11}$$

Since v_p and ω_p are virtually constant in magnitude, T_e and Q_p control via i_{sq} and i_{sd} is intrinsically decoupled according to (10) and (11) and can be realised as illustrated in Fig. 3. Any inductance knowledge inaccuracies can be handled by the correctly tuned PI gains.

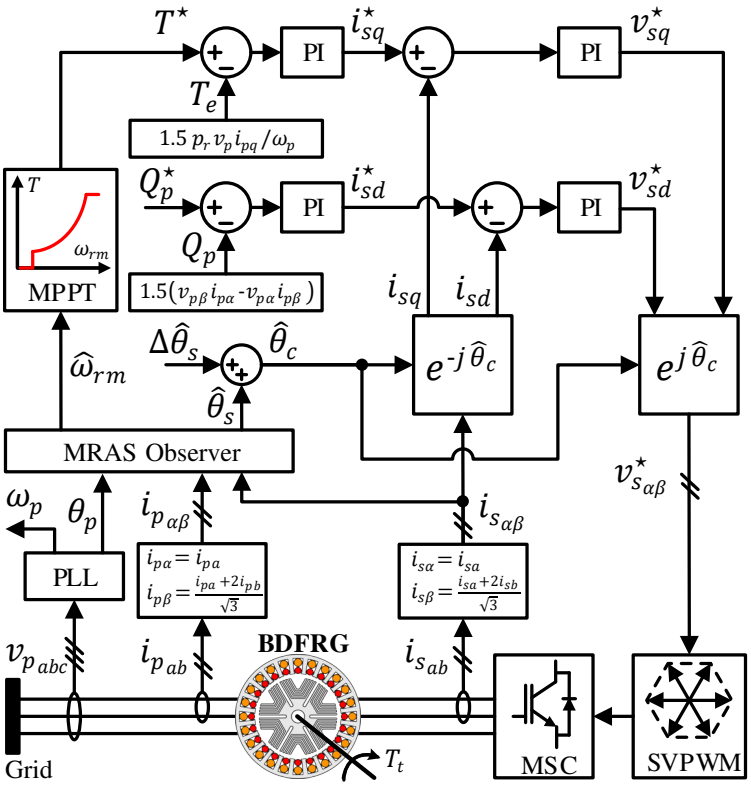

Figure 3: The BDFRG sensorless voltage oriented controller.

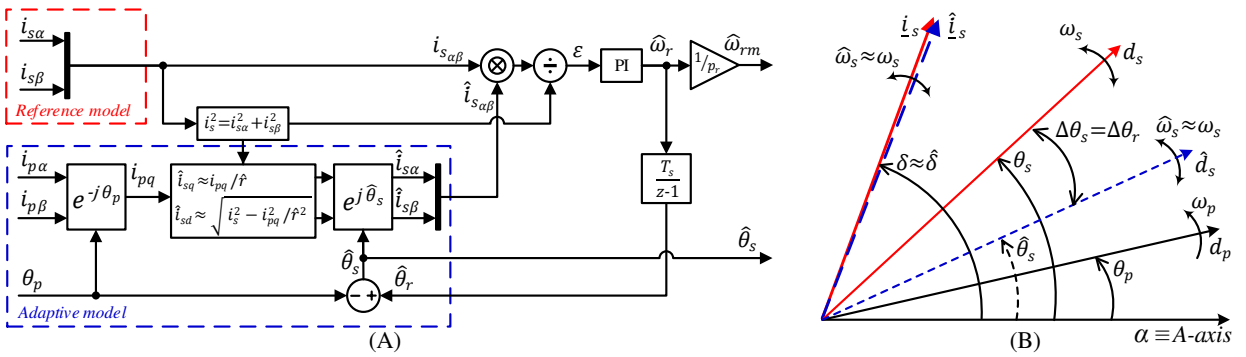

Figure 4: The parameter-free MRAS observer: A) Block scheme; B) Phasor diagram with key space vectors and reference frames.

4. Angular Velocity and Position Observer

The MRAS observer layout is presented in Fig. 4A. The reference model is highly accurate as being purely based on the secondary current measurements to derive the respective $i_{s\alpha}$ and $i_{s\beta}$ outputs in a stationary $\alpha-\beta$ frame as formulated in Fig. 3 for a Y-connected winding with a positive phase sequence and no neutral connection.

Considering (9) and Fig. 2, the magnetically coupled secondary currents in the d_p-q_p frame, $\hat{i}_{mq}$ and $\hat{i}_{md}$, are the same as the source components in the d_s-q_s frame, $\hat{i}_{sq}$ and $\hat{i}_{sd}$. They can be estimated from the measurable i_{pq} and i_{pd} in the d_p-q_p frame applying (5) in the following manner:

$$\hat{i}_{mq}=\hat{i}_{sq}=\frac{-\lambda_{pq}+\hat{L}_p i_{pq}}{\hat{L}_m}\approx\frac{\hat{L}_p}{\hat{L}_m}i_{pq}=\frac{i_{pq}}{\hat{r}} \tag{12}$$

$$\hat{i}_{md}=\hat{i}_{sd}=\frac{\lambda_{pd}-\hat{L}_p i_{pq}}{\hat{L}_m}\approx\frac{v_p}{\omega_p\hat{L}_m}-\frac{i_{pd}}{\hat{r}} \tag{13}$$

$$i_{pd}+ji_{pq}=(i_{p\alpha}+ji_{p\beta})e^{-j\theta_p} \tag{14}$$

where $\hat{L}_m$ and $\hat{L}_p$ are the inductance values identified by off-line testing ($\hat{r}=\hat{L}_m/\hat{L}_p$) [32], whereas $i_{p\alpha}$ and $i_{p\beta}$ are obtained from the measured primary currents as in Fig. 3.

In order to minimise the parameter dependence and potential sensitivity issues, $\hat{i}_{sd}$ is estimated applying (12) and (14) as follows:

$$\hat{i}_{sd}=\sqrt{i_s^2-\hat{i}_{sq}^2}\approx\sqrt{i_s^2-i_{pq}^2/\hat{r}^2} \tag{15}$$

where i_s is the measured secondary current magnitude. Doing so, $\hat{i}_{sd}$ is now only dependent on a 'more predictable' inductance ratio ($\hat{r}$), and not additionally on $\hat{L}_m$ has (13) been used.

A usual d_s-q_s to $\alpha-\beta$ frame conversion, $\underline{i}_{\alpha\beta}=\underline{i}_{dq}e^{j\theta_s}$, can now be applied to calculate:

$$\hat{i}_{s\alpha}=\hat{i}_{sd}\cos(\hat{\theta}_r-\theta_p)-\hat{i}_{sq}\sin(\hat{\theta}_r-\theta_p) \tag{16}$$

$$\hat{i}_{s\beta}=\hat{i}_{sd}\sin(\hat{\theta}_r-\theta_p)+\hat{i}_{sq}\cos(\hat{\theta}_r-\theta_p) \tag{17}$$

where $\hat{\theta}_s=\hat{\theta}_r-\theta_p$ (Fig. 4B) and $\hat{\theta}_r=p_r\hat{\theta}_{rm}$ are the secondary frame and rotor 'electrical' positions estimated using the angular version of (1):

$$\theta_r=p_r\theta_{rm}=\theta_p+\theta_s \tag{18}$$

By applying (18), it can be easily shown that the $\hat{\theta}_r$ and $\hat{\theta}_s$ errors are equal:

$$\Delta\theta_r=\theta_r-\hat{\theta}_r=(\theta_s+\theta_p)-(\hat{\theta}_s+\theta_p)=\theta_s-\hat{\theta}_s=\Delta\theta_s \tag{19}$$

The normalised error of the adaptive model is defined as:

$$\varepsilon = \frac{\hat{\underline{i}}_s \times \underline{i}_s}{i_s^2} = \frac{\hat{\underline{i}}_s \cdot \underline{i}_s}{i_s^2} \cdot \sin\Delta\delta = \frac{\hat{i}_{s\alpha} i_{s\beta} - \hat{i}_{s\beta} i_{s\alpha}}{i_{s\alpha}^2 + i_{s\beta}^2} \tag{20}$$

where $\Delta\delta = \delta - \hat{\delta}$ is the angular misalignment between the actual ($\underline{i}_s$) and estimated ($\hat{\underline{i}}_s$) secondary-current vectors. This is being driven to zero by feeding-back the enhanced $\hat{\theta}_r$ as shown in Fig. 4B. Once $\Delta\delta \approx 0$, then $\tan\hat{\delta} = \hat{i}_{s\beta}/\hat{i}_{s\alpha} \approx \tan\delta = i_{s\beta}/i_{s\alpha}$ i.e. $\hat{i}_s$ and i_s nearly overlap both rotating at $\hat{\omega}_s \approx \omega_s$.

4.1. Small signal model and stability analysis

The overall stability of a MRAS observer depends on the adaptation mechanism to guarantee the convergence of the estimated quantity to its actual value. The hyper-stability concept is applied to different adaptation mechanisms structures to provide global asymptotic stability for the MRAS observer [33, 34]. The dynamic response of a particular MRAS, with a proven stable adaptation technique, can be analysed by linearising the observer around a selected operating point [35]. The small signal model of (20), around the $\Delta\delta \approx 0$, $\cos\Delta\delta \approx 1$, $\hat{i}_s \approx i_s$ steady-state point, is:

$$\begin{aligned}\frac{d\varepsilon}{dt} &= \frac{\hat{i}_s \cdot i_s}{i_s^2}\cos\Delta\delta\left(\frac{d\delta}{dt} - \frac{d\hat{\delta}}{dt}\right) \approx \frac{d\delta}{dt} - \frac{d\hat{\delta}}{dt} \\ &\approx \omega_s - \hat{\omega}_s = (\omega_r - \omega_p) - (\hat{\omega}_r - \omega_p) = \Delta\omega_r \end{aligned} \tag{21}$$

$$\varepsilon \approx \int (\omega_r - \hat{\omega}_r)dt = \frac{\omega_r - \hat{\omega}_r}{s} = p_r\frac{\Delta\omega_{rm}}{s} \tag{22}$$

The above relationships clearly indicate that a key factor for the observer stability is the high accuracy of $\hat{\omega}_r$ (i.e $\Delta\omega_r \approx 0 \Rightarrow \dot{\varepsilon} \approx 0$). The PI controller, shown in Fig. 5, is designed using (22) to obtain the $\hat{\omega}_r$ resulting in $\varepsilon \approx 0$. Adaptive PI tuning under variable loading conditions is provided by the i_s^2 division term in (20).

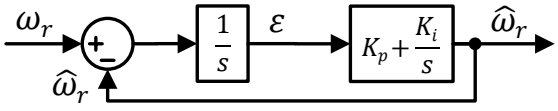

Figure 5: The MRAS small signal model.

4.2. Sensitivity studies and position error compensation technique

The observer ensures that $\varepsilon \approx 0$, hence $\Delta\delta \approx 0$ (i.e. $\hat{\delta} \approx \delta$), no matter the inductance ratio mismatch according to (20)-(22). Using Fig. 4B and (15), one can write the following relationship in the $\hat{d}_s - \hat{q}_s$ (control) frame:

$$\frac{\hat{i}_{sq}}{\hat{i}_{sd}} = \tan(\delta - \hat{\theta}_s) = \frac{\hat{i}_{sq}}{\sqrt{i_s^2 - \hat{i}_{sq}^2}} \tag{23}$$

Differentiating (23) with $d\delta \approx \Delta\delta \approx 0$ it can be obtained that:

$$\frac{d\hat{\theta}_s}{\cos^2(\delta - \hat{\theta}_s)} = \left[1 + \tan^2(\delta - \hat{\theta}_s)\right] d\hat{\theta}_s = -\frac{i_s^2 \cdot d\hat{i}_{sq}}{(i_s^2 - \hat{i}_{sq}^2)^{3/2}} \tag{24}$$

Substituting for (23), (24) may be simplified to:

$$d\hat{i}_{sq} \approx -\sqrt{i_s^2 - \hat{i}_{sq}^2} \cdot d\hat{\theta}_s \tag{25}$$

The above expression can be further rearranged by applying $\hat{r} \cdot d\hat{i}_{sq} = -\hat{i}_{sq} \cdot d\hat{r}$ coming from (12) as follows:

$$\frac{d\hat{\theta}_s}{d\hat{r}} \approx \frac{\Delta\hat{\theta}_s}{\Delta\hat{r}} = \frac{\hat{i}_{sq}}{\hat{r} \cdot \hat{i}_{sd}} = \frac{i_{pq}}{\hat{r} \cdot \sqrt{\hat{r}^2 \cdot i_s^2 - i_{pq}^2}} \leq 0 \tag{26}$$

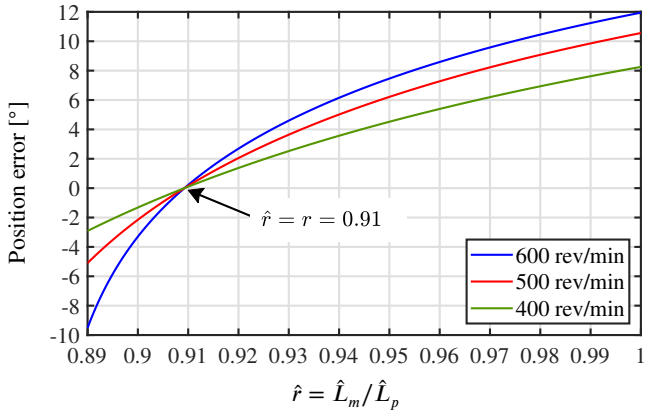

Figure 6: Graphical representation of (26) showing the observer sensitivity to $\hat{r}$.

where $\Delta\hat{r} \approx r - \hat{r}$. The rate of change of $\hat{\theta}_s$ is obviously decreasing with $\hat{r}$, being the slowest for the maximum empirical value of $\hat{r} \approx 0.95$ common with commercial DFIGs [36], when $|\Delta\hat{\theta}_s|$ is the smallest for a given $|\Delta\hat{r}|$. The sensitivity to $\hat{r}$ is presented in Fig. 6, which illustrates the position estimation error (i.e. the frame misalignment) at various operating speeds.

Under this practical assumption, which forms the basis of the proposed parameter independent observer and sensorless controller designs in Figs. 4A and 3, both (15) and (26) get purely based on i_s and i_{pq}, which can be obtained directly from measurements using the conventional transformations shown in Fig. 3. With optimally designed BDFRGs, the leakage flux is predominantly located in the secondary (and not primary) winding rendering the actual $r > 0.85$ up to $r_{max} \approx 0.95$ at most as for DFIGs of similar rating [13]. So, for $\Delta\hat{r} \approx -0.1$ or higher (i.e. less negative), (26) can serve well for $\Delta\hat{\theta}_s$ predictions. Such an approach has been implemented on-line to compensate the observed $\hat{\theta}_s$ as illustrated in Fig. 3. This has significantly improved the observer accuracy and quality of response as will be demonstrated in the following section.

5. Simulation and Experimental Results

The sensorless scheme in Fig. 3 is simulated and validated by laboratory tests using the BDFRG turbine specifications from Table 2 and Fig. 7. Note that T_e has been controlled for the MPPT as being directly responsible for the rotor speed variations. This should reinforce the drive train stability under the open-loop speed control conditions. The Simulink® studies have been made realistic by including: discrete-time implementation, high frequency white noise and transducer dc offset in measurements, and detailed IGBT converter models. The BDFRG design particulars can be found in [13].

Table 2
The 1.5 MW BDFRG ratings and parameters

Stator voltages (V rms)	$V_p = 690$	$V_s = 230$
Stator currents (kA rms)	$I_p = 1.1$	$I_s = 1.2$
Winding resistance (mΩ)	$R_p = 7$	$R_s = 14.2$
Winding self-inductance (mH)	$L_p = 4.9$	$L_s = 5.7$
Mutual inductance (mH)	$L_m = 4.5$	
Primary and secondary pole-pairs	$p_p = 4$	$p_s = 2$
Generator and turbine speed (rev/min)	600	20

The performance is examined on the Hardware-In-the-Loop (HIL) system shown in Fig. 8. The C-code is compiled in dSPACE® [37] from the Simulink® model using the Real-Time Workshop® and run at 10 kHz switching rate of the space-vector-pulse-width-modulated (SVPWM) converter. The dynamic model of the BDFRG-based wind turbine

with its associated controller shown in Fig. 3 have been implemented in the PowerPC 750GX® processor at 100 μs sampling time. The real-time generated voltage and current values are provided for the MRAS observer estimation of speed and position to achieve the promising sensorless control performance for large-scale wind power applications.

The BDFRG response to wind speed step changes in Fig. 9 has been considered to expose the controller to dynamically the most challenging circumstances. he rotor speed variations are relatively slow due to a high inertia of the BDFRG wind turbine. The $\hat{\omega}_{rm}$ estimates used to generate the MPPT torque reference ($T^\star$) 100 rev/min around, and down to, the synchronous speed (500 rev/min), as per Fig. 7, are observed with negligible error. The same applies to $\hat{\delta}$ since the mean $\Delta\delta \approx 0$ throughout. Such a high estimation quality is expected and represents the observer trademark as discussed in Section 4. However, the accuracy of $\hat{\theta}_s$ is compromised to some extent by the underlying $\hat{r} \approx 0.95$ assumption, and it is getting worse with the speed increase, culminating in the super-synchronous mode of most practical importance. This undesirable trend can be explained by the rising $|T_e|$ and $|i_{pq}|$ levels in (26), according to Fig. 7 and (10). The corresponding Δi_{sd} and Δi_{sq} can be formulated by means of Fig. 4B and small-angle approximations as follows:

$$\begin{aligned}\Delta i_{sd} &= i_s \cdot [\cos(\delta - \theta_s) - \cos(\delta - \hat{\theta}_s)] \\ &= 2 i_s \sin\frac{\Delta\theta_s}{2} \sin(\delta - \hat{\theta}_s - \frac{\Delta\theta_s}{2}) \approx \Delta\theta_s \cdot i_{sq} \end{aligned} \tag{27}$$

$$\begin{aligned}\Delta i_{sq} &= i_s \cdot [\sin(\delta - \theta_s) - \sin(\delta - \hat{\theta}_s)] \\ &= 2 i_s \sin\frac{-\Delta\theta_s}{2} \cos(\delta - \hat{\theta}_s - \frac{\Delta\theta_s}{2}) \approx -\Delta\theta_s \cdot i_{sd} \end{aligned} \tag{28}$$

A cross-coupling has been introduced by the speed dependent $\Delta\theta_s$. The effects are much more pronounced in (27) than (28) due to the comparatively larger $|i_{sq}|$ magnitudes, especially at higher rotor speeds. Furthermore, both $|\Delta i_{sd}|$ and $|\Delta i_{sq}|$ are nearly proportional to $\Delta\theta_s$, so there is a great deal of similarity in their behaviour and spread over the entire speed range.

Despite the fact that the previously addressed absolute error propagation is not suitable for the BDFRG's most efficient super-synchronous operation, the extremes are relatively small to cause any visible performance degradation. It can be seen from Fig. 9 that Q_p, hence i_{sd}, are effectively controlled for the unity power factor (i.e. $Q_p^\star = 0$) with the secondary winding taking over completely the machine magnetisation from the primary side as $i_{pd} = 0$ given (11). The i_{sq} and i_{pq} waveforms are essentially scaled replicas of the closely related P_p and T_e ones considering (10). They don't seem affected by the sudden variations instigated in the Q_p, and further reflected upon the i_{sd} and i_{pd} counterparts, to demonstrate the excellent disturbance rejection capabilities of the PI regulators. Notice that the i_{sd} step increases in response to the $Q_p < 0$ dips (i.e. for the over-excited BDFRG producing $|Q_p|$ by analogy to a classical wound field synchronous generator) lead to a favourable decline of $\Delta\theta_s$ according to (26).

It is also worth pointing out in relation to Fig. 9 that the MPPT has been achieved indirectly through torque control. For instance, the desired total power output at the rated wind speed of 12 m/s is $P_m = -1.5$ MW as shown in absolute

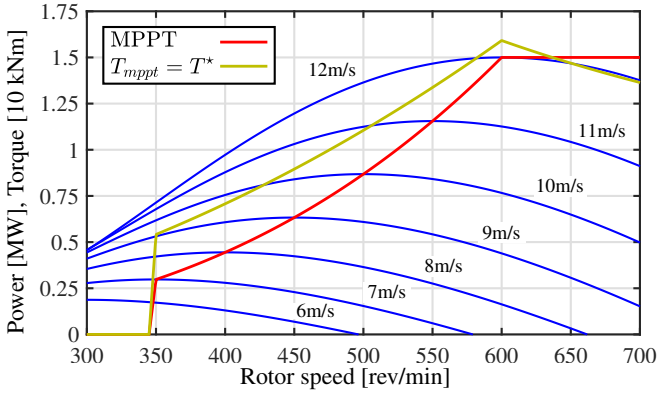

Figure 7: Turbine characteristics for various wind and BDFRG speeds, including the MPPT torque and power profiles.

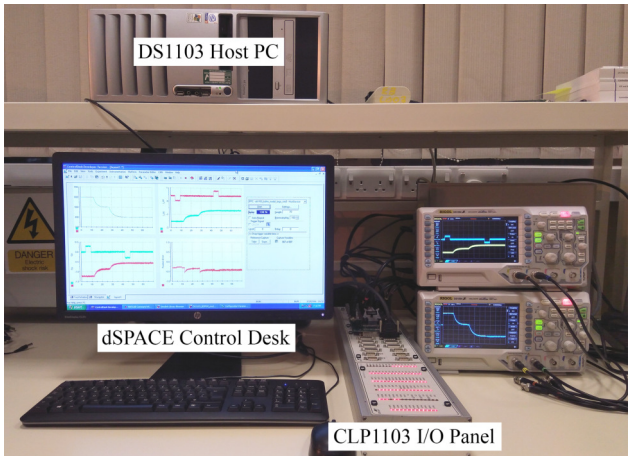

Figure 8: HIL instrumentation for the BDFRG WECS emulation.

sense in Fig. 7. The secondary frequency at 600 rev/min for $a = 1.5$ and $f_p = 50$ Hz in (3) is $f_s = 10$ Hz. Thus, the primary winding input should be $P_p = -1.25$ MW from (2), which can be verified from the P_p curves. The remaining 0.25 MW is delivered to the grid via the converter i.e. $P_s \approx 0.17 P_m$. Note the secondary phase sequence reversal from positive to negative (i.e. $\omega_s < 0$ in Fig. 2) accompanied by the speed mode transition from super to sub-synchronous. For this reason, at 8 m/s and 400 rev/min, $f_s = -10$ Hz in (2) making $P_p \approx -0.56$ MW for $P_m \approx -0.45$ MW. The secondary side provides the power balance, but now consuming 0.11 MW i.e. $P_s \approx 0.24|P_m|$. Finally, there is a very good correlation between the oscillograms, captured as shown in Fig. 8, and the simulated subplots presented back-to-back in Fig. 9.

5.1. Enhanced position error compensated control

The erroneous rotor position estimates manifest themselves through a secondary (control) frame misalignment ($\Delta\theta_s$) as depicted in Fig. 4B producing the current feedback inaccuracies as a by-product. The latter are mainly in the d_s-axis (i.e. $|\Delta i_{sd}| >> |\Delta i_{sq}|$) as a consequence of the cross-coupling incurred, which can be approximately quantified by (27) and (28). Although these estimation errors are not significant even at super-synchronous speeds of the considered BDFRG turbine having $r \approx 0.92$ (Table 2) as shown in Fig. 9, they can be further reduced for superior performance by using (26) to generate a $\Delta\hat{\theta}_s$ compensation term for $\hat{r} \approx 0.95$ as mentioned in Section 4.2 and implemented in Fig. 3. As the exact inductance ratio (r) is assumed unknown for control purposes, but is typically between 0.85 and 0.95 for most BDFRGs, $\Delta\hat{r} = -0.1$ and $\Delta\hat{r} = -0.05$ have been chosen as reasonable mid to low r range options to demonstrate the effectiveness of the proposed method. The comparative test results are displayed in Fig. 10. The $|\Delta\theta_s|$, and in turn $|\Delta i_{sd,q}|$, values from Fig. 9 have notably decreased, the biggest % reduction (more than twice) for either case study occurring where needed the most i.e. at the rated point, and particularly with $\Delta\hat{r} = -0.05$ as expected for the example BDFRG.

Similar comparisons without or with $\Delta\theta_s$ correction for the same $\Delta\hat{r}$ as in Fig. 10 can be done from Fig. 11 for a hypothetical BDFRG with the higher primary leakage flux i.e. the lower r than in Table 2. Unlike the situation in Fig. 9, the uncompensated error levels are further elevated since the $\hat{r}$ mismatch is now much higher. A considerable accuracy improvement has been achieved with $\Delta\theta_s$ compensation for $\Delta\hat{r} = -0.1$. The $|\Delta\theta_s|$, hence $|\Delta i_{sd,q}|$, have fallen nearly by a factor of 3, being approximately a half of those experienced for $\Delta\hat{r} = -0.05$ throughout.

Judging by the comparative studies of Figs. 10 and 11, summarised in Table 3, $\Delta\hat{r} = -0.1$ appears to be a more representative compensation solution overall, offering good quality estimates and performance for a wider range of BDFRGs. This is also apparent from Fig. 12 showing oscilloscope recordings of the decoupled sensorless T_e, Q_p and current control responses of the BDFRG (Table 2) to naturalistic wind speed variations [38].

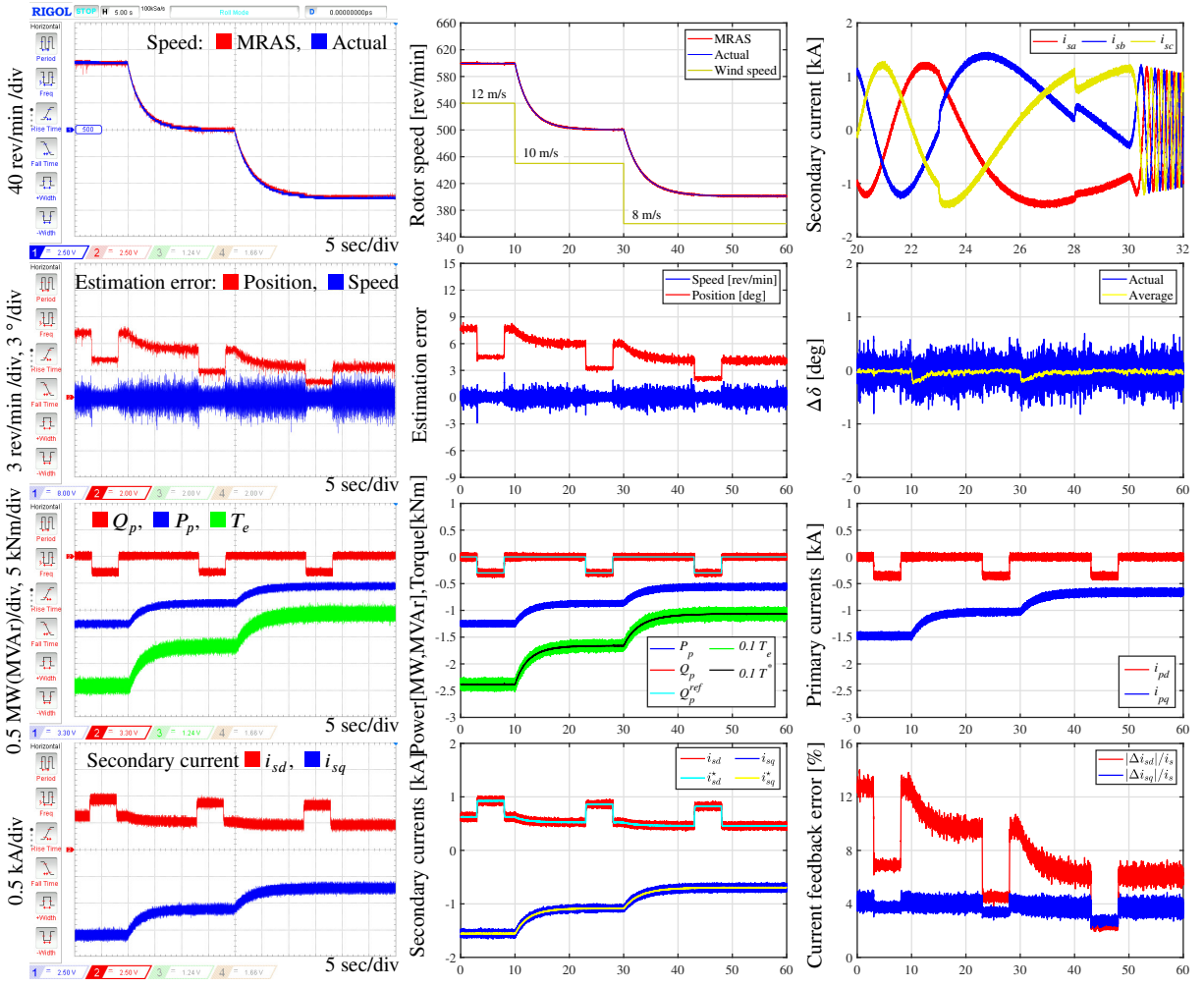

Figure 9: Comparative experimental and simulation studies of the BDFRG operation with uncompensated MRAS.

6. Conclusions

An innovative, parameter independent MRAS based estimation technique for sensorless control of torque and reactive power (Q_p) of large BDFRG wind turbines has been presented and validated by realistic simulations and experimentally. The results produced for a custom 1.5 MW design have demonstrated the controller ability to provide mutually decoupled MPPT and Q_p responses to variable Q_p and loading conditions. Such performance has been afforded by the precise rotor speed estimates of the MRAS observer having strong advantages over the existing counterparts reported in the open literature. These include highly reliable reference and closed-loop adaptive models utilising measurements only: the former of the secondary currents, and the latter of the primary voltages and currents at fixed line frequency. The valid approximations made going to the essence of the BDFRG operation, coupled with the properly tuned PI gains derived from a small-signal analysis, have allowed to: (1) by-pass the L_m/L_p dependence of the suitably tailored adaptive model; (2) significantly improve the observer accuracy by implementing a position error predictive scheme for on-line compensation of the secondary (control) frame misalignment; (3) enhance the stability and robustness of the observer/control algorithm by making it truly machine parameter-free. The supporting sensitivity studies to mismatches in the BDFRG inductance ratio have verified the effectiveness of the proposed estimation approach by comprehensive simulations and HIL experiments for fast wind speed changes including realistic wind speed profiles.

The above arguments are stimulating for continuing BDFRG research as a prospective, medium-speed DFIG

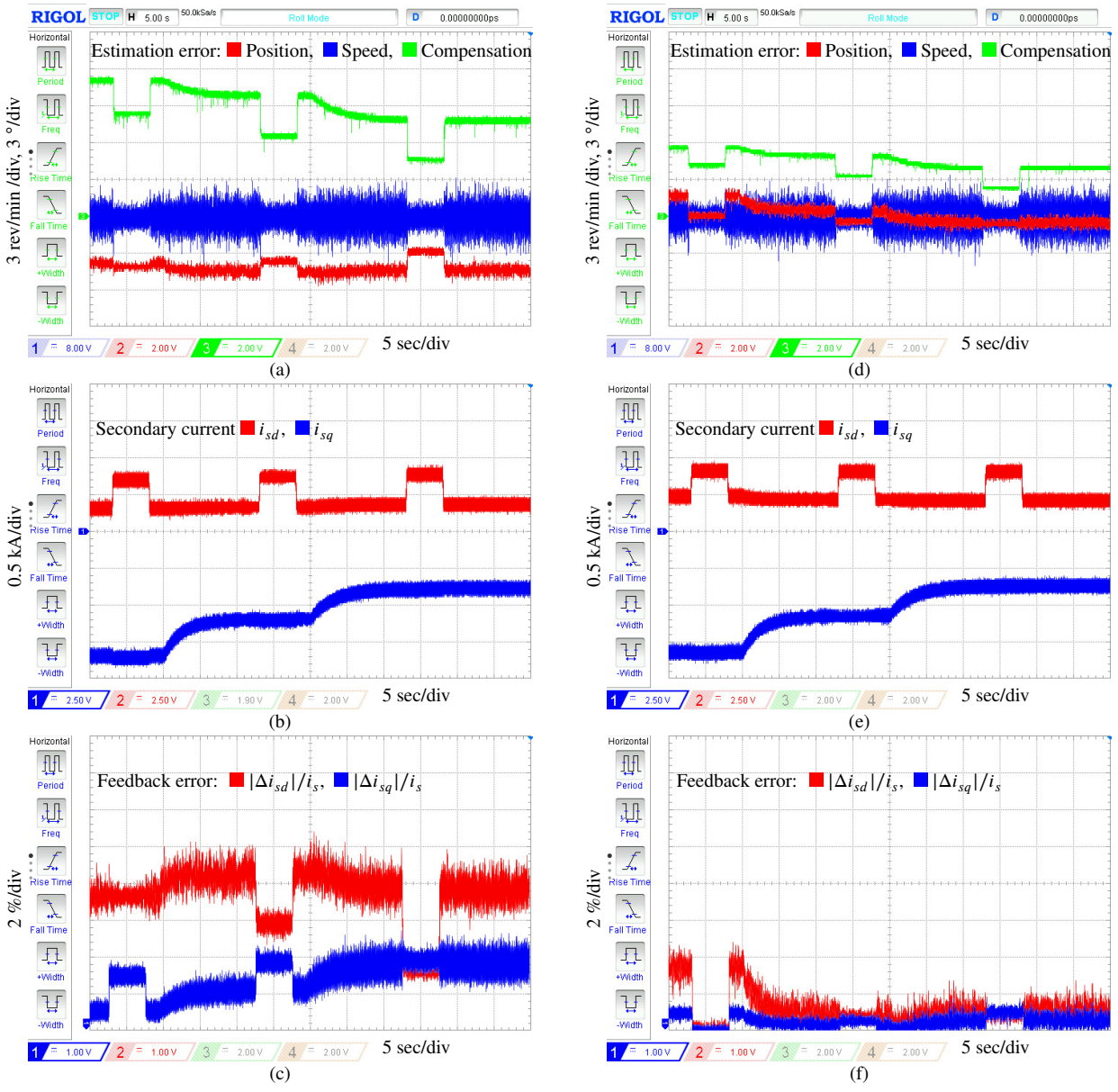

Figure 10: Real-time performance with control frame misalignment compensation for: (a-c) $\Delta\hat{r} = -0.1$; (d-f) $\Delta\hat{r} = -0.05$.

substitute. Its maintenance-free sensorless operation with a more reliable 2-stage gearbox should be attractive cost saving factors to consider for grid-connected wind power applications.

References

[1] H. Jadhav, R. Roy, A comprehensive review on the grid integration of doubly fed induction generator, International Journal of Electrical Power and Energy Systems 49 (2013) 8–18.

[2] C. Mehdipour, A. Hajizadeh, I. Mehdipour, Dynamic modeling and control of DFIG-based wind turbines under balanced network conditions, International Journal of Electrical Power and Energy Systems 83 (2016) 560–569.

[3] J. Carroll, A. McDonald, D. McMillan, Reliability comparison of wind turbines with DFIG and PMG drive trains, IEEE Transactions on Energy Conversion 30 (2) (2015) 663–670.

[4] K. Fischer, K. Pelka, A. Bartschat, B. Tegtmeier, D. Coronado, C. Broer, J. Wenske, Reliability of power converters in wind turbines:

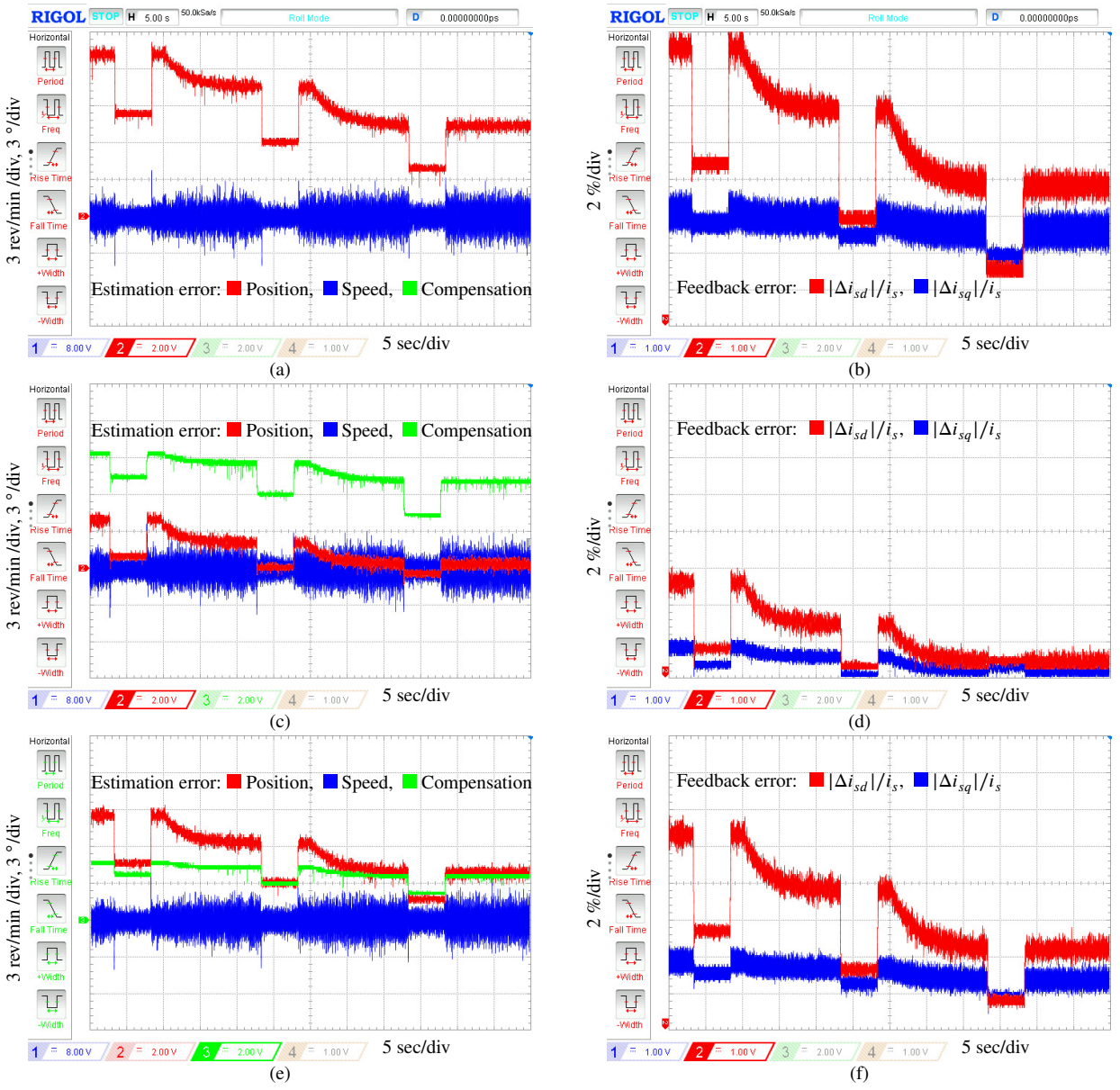

Figure 11: Estimation quality metrics for the BDFRG with $r = 0.87$ and the control frame misalignment: (a-b) uncompensated, (c-d) compensated for $\Delta\hat{r} = -0.1$; (e-f) compensated for $\Delta\hat{r} = -0.05$.

Exploratory analysis of failure and operating data from a worldwide turbine fleet, IEEE Transactions on Power Electronics 34 (7) (2019) 6332–6344.

[5] J. Wei, C. Li, Q. Wu, B. Zhou, D. Xu, S. Huang, MPC-based DC-link voltage control for enhanced high-voltage ride-through of offshore DFIG wind turbine, International Journal of Electrical Power and Energy Systems 126 (2021) 1–11.

[6] M. Cheng, P. Han, G. Buja, M. G. Jovanovic, Emerging multiport electrical machines and systems: Past developments, current challenges, and future prospects, IEEE Transactions on Industrial Electronics 65 (7) (2018) 5422–5435.

[7] F. Zhang, H. Wang, G. Jia, D. Ma, M. G. Jovanovic, Effects of design parameters on performance of brushless electrically excited synchronous reluctance generator, IEEE Transactions on Industrial Electronics 65 (11) (2018) 9179–9189.

[8] J. Liang, K. Zhang, A. Al-Durra, D. Zhou, A novel fault diagnostic method in power converters for wind power generation system, Applied Energy 266 (2020) 114851.

[9] M. F. Hsieh, Y. H. Chang, D. Dorrell, Design and analysis of brushless doubly-fed reluctance machine for renewable energy applications, IEEE Transactions on Magnetics 52 (7) (July 2016).

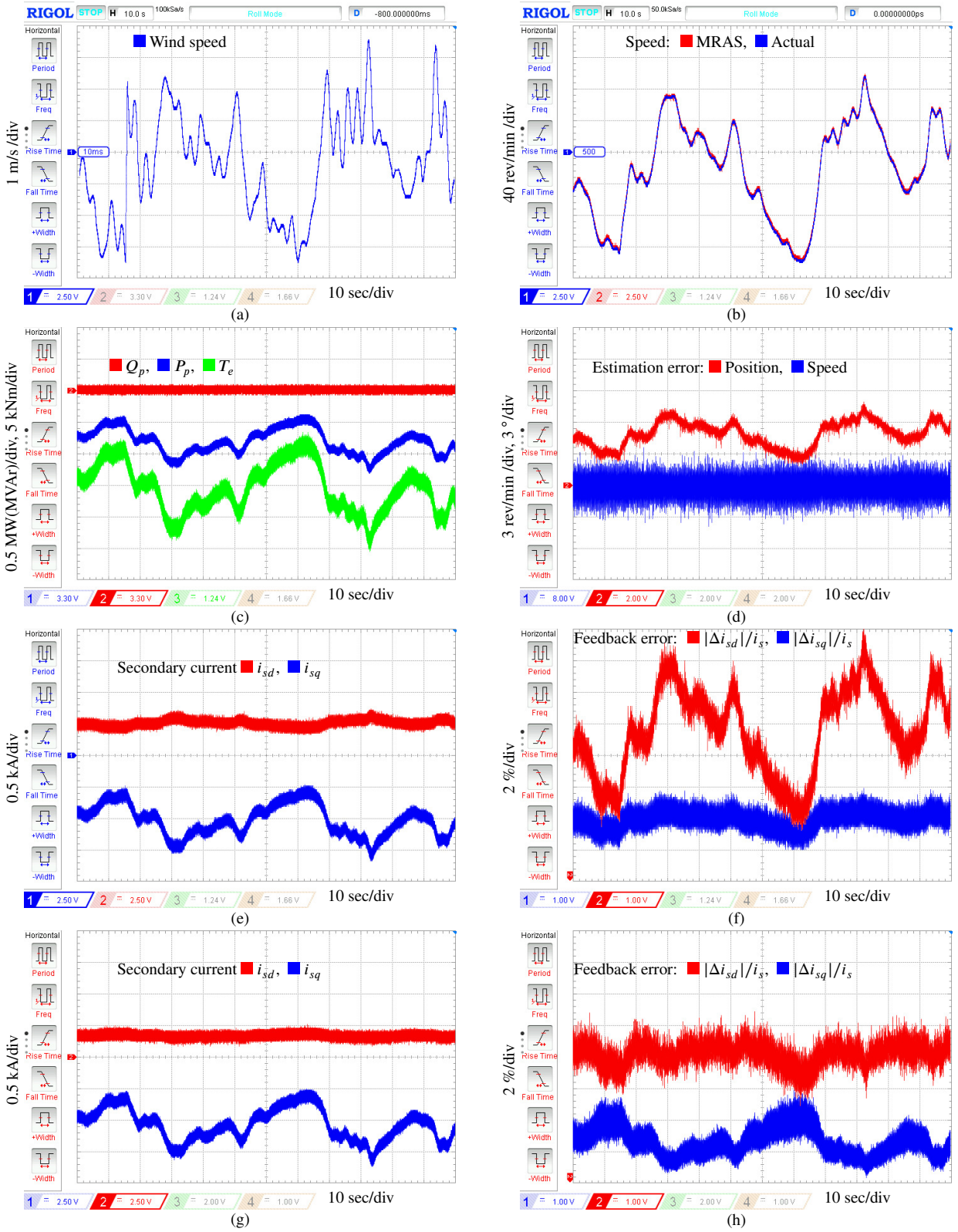

Figure 12: Oscilloscope traces showing BDFRG control performance for realistic wind speed fluctuations with: (a-f) uncompensated; (g-h) compensated observer output using $\Delta\hat{r} = -0.1$ for position error calculations.

Table 3
Average position estimation errors at $Q_p = 0$.

Method / Speed	uncompensated	compensated $\Delta\hat{r} = -0.1$	compensated $\Delta\hat{r} = -0.05$	
400 rev/min	4.09°	-4.19°	-0.44°	$r = 0.91$
500 rev/min	5.88°	-3.76°	1.02°	
600 rev/min	7.27°	-3.45°	2.04°	
400 rev/min	7.45°	0.88°	4.15°	$r = 0.87$
500 rev/min	10.88°	2.25°	6.54°	
600 rev/min	13.20°	4.03°	8.70°	

[10] M. E. Mathekga, S. Ademi, R. A. McMahon, Brushless doubly fed machine magnetic field distribution characteristics and their impact on the analysis and design, IEEE Transactions on Energy Conversion 34 (4) (2019) 2180–2188.

[11] F. Zhang, S. Yu, Y. Wang, S. Jin, M. G. Jovanovic, Design and performance comparisons of brushless doubly-fed generators with different rotor structures, IEEE Transactions on Industrial Electronics 66 (1) (2019) 631–640.

[12] M. Moazen, R. Kazemzadeh, M.-R. Azizian, Mathematical modeling and analysis of brushless doubly fed reluctance generator under unbalanced grid voltage condition, International Journal of Electrical Power and Energy Systems 83 (2016) 547–559.

[13] A. Attya, S. Ademi, M. Jovanovic, O. Anaya-Lara, Frequency support using doubly fed induction and reluctance wind turbine generators, International Journal of Electrical Power and Energy Systems 101 (2018) 403–414.

[14] F. Mazouz, S. Belkacem, I. Colak, S. Drid, Y. Harbouche, Adaptive direct power control for double fed induction generator used in wind turbine, International Journal of Electrical Power and Energy Systems 114 (2020) 1–11.

[15] M. Abolvafaei, S. Ganjefar, Maximum power extraction from fractional order doubly fed induction generator based wind turbines using homotopy singular perturbation method, International Journal of Electrical Power and Energy Systems 119 (2020) 1–17.

[16] S. Ademi, M. Jovanovic, Vector control methods for brushless doubly fed reluctance machines, IEEE Transactions on Industrial Electronics 62 (1) (2015) 96–104.

[17] S. Ademi, M. Jovanovic, M. Hasan, Control of brushless doubly-fed reluctance generators for wind energy conversion systems, IEEE Transactions on Energy Conversion 30 (2) (2015) 596–604.

[18] M. Morawiec, K. Blecharz, A. Lewicki, Sensorless rotor position estimation of doubly fed induction generator based on backstepping technique, IEEE Transactions on Industrial Electronics 67 (7) (2020) 5889–5899.

[19] A. T. Nguyen, D. C. Lee, Sensorless control of DFIG wind turbine systems based on SOGI and rotor position correction, IEEE Transactions on Power Electronics 36 (5) (2020) 5486 – 5495.

[20] K. Xiahou, X. Lin, Y. Liu, Q. H. Wu, Robust rotor-current sensorless control of doubly fed induction generators, IEEE Transactions on Energy Conversion 33 (2) (2018) 897–899.

[21] U. Shipurkar, T. D. Strous, H. Polinder, J. A. Ferreira, A. Veltman, Achieving sensorless control for the brushless doubly fed induction machine, IEEE Transactions on Energy Conversion 32 (4) (2017) 1611–1619.

[22] M. Jovanovic, S. Ademi, R. Binns, Sensorless variable speed operation of doubly-fed reluctance wind generators, IET Renewable Power Generation (2020) 1–10.

[23] S. Ademi, M. G. Jovanovic, H. Chaal, W. Cao, A new sensorless speed control scheme for doubly fed reluctance generators, IEEE Transactions on Energy Conversion 31 (3) (2016) 993–1001.

[24] K. Kiran, S. Das, M. Kumar, A. Sahu, Sensorless speed control of brushless doubly-fed reluctance motor drive using secondary flux based MRAS, Electric Power Components and Systems 46 (6) (2018) 701–715.

[25] M. Kumar, S. Das, K. Kiran, Sensorless speed estimation of brushless doubly-fed reluctance generator using active power based MRAS, IEEE Transactions on Power Electronics 34 (8) (2019) 7878–7886.

[26] M. R. Agha Kashkooli, M. G. Jovanovic, S. Ademi, Sensorless power control of doubly-fed reluctance wind turbine generators using a current-based MRAS estimator, 2020 International Symposium on Power Electronics, Electrical Drives, Automation and Motion (SPEEDAM) (2020) 65–70.

[27] M. R. Agha Kashkooli, M. G. Jovanovic, A MRAS observer for sensorless operation of grid-connected bdfrg wind turbines, 2020 IEEE 29th International Symposium on Industrial Electronics (ISIE) (2020) 1517–1522.

[28] M. R. Agha Kashkooli, M. G. Jovanovic, Sensorless MRAS control of brushless doubly-fed reluctance generators for wind turbines, in: 2020 International Conference on Electrical Machines (ICEM), Vol. 1, 2020, pp. 2202–2208.

[29] M. R. Agha Kashkooli, M. Jovanovic, Sensorless MRAS control of emerging doubly-fed reluctance wind generators, IET Renewable Power Generation (2021) 1–15.

[30] R. E. Betz, M. G. Jovanovic, Theoretical analysis of control properties for the brushless doubly fed reluctance machine, IEEE Transactions on Energy Conversion 17 (3) (2002) 332–339.

[31] R. E. Betz, M. G. Jovanovic, Introduction to the space vector modelling of the brushless doubly-fed reluctance machine, Electric Power Components and Systems 31 (8) (2003) 729–755.

[32] D. Gay, R. E. Betz, D. Dorrell, A. Knight, Brushless doubly fed reluctance machine testing for parameter determination, IEEE Transactions on Industry Applications 55 (3) (2019) 2611–2619.